Commensurate magnetic structures of $R\mathrm{Mn_2O_5}$ (R=Y,Ho,Bi) determined by single-crystal neutron diffraction

C. Vecchini,[1,2] L. C. Chapon,[1] P. J. Brown,[3] T. Chatterji,[3] S. Park,[4] S-W. Cheong,[4] and P. G. Radaelli[1]
[1]*ISIS Facility, Rutherford Appleton Laboratory, Chilton, Didcot, Oxfordshire OX11 0QX, United Kingdom*
[2]*Institute of Electronic Structure and Laser, Foundation for Research and Technology-Hellas, Vassilika Vouton, Heraklion, 711 10 Crete, Greece*
[3]*Institut Laue-Langevin, 6, Rue Jules Horowitz, Boîte Postale 156, 38042 Grenoble Cedex 9, France*
[4]*Rutgers Center for Emergent Materials and Department of Physics and Astronomy, Rutgers University, Piscataway, New Jersey 08854, USA*

(Received 10 October 2007; revised manuscript received 25 January 2008; published 18 April 2008)

Precise magnetic structures of $R\mathrm{Mn_2O_5}$, with R=Y,Ho,Bi in the commensurate and/or ferroelectric regime, have been determined by single-crystal neutron diffraction. For each system, the integrated intensities of a large number of independent magnetic Bragg reflections have been measured, allowing unconstrained least-squares refinement of the structures. The analysis confirms the previously reported magnetic configuration in the *ab* plane, in particular, the existence of zigzag antiferromagnetic chains. For the Y and Ho compounds, additional weak magnetic components parallel to the *c* axis were detected, which are modulated in phase quadrature with the *a*-*b* components. This component is extremely small in the $\mathrm{BiMn_2O_5}$ sample, therefore supporting symmetric exchange as the principal mechanism inducing ferroelectricity. For $\mathrm{HoMn_2O_5}$, a magnetic ordering of the Ho moments was observed, which is consistent with a superexchange interaction through the oxygens. For all three compounds, the point symmetry in the magnetically ordered state is *m*2*m*, allowing the polar *b* axis found experimentally.

DOI: 10.1103/PhysRevB.77.134434 PACS number(s): 75.25.+z, 77.80.−e, 61.05.fm

I. INTRODUCTION

Materials in which there is strong interplay between ferroelectric and magnetic ordering are attracting current interest due to the possibility of controlling the electric polarization by application of a magnetic field or conversely the magnetization with an electric field. In the last few years, studies have been focused on systems, such as $\mathrm{TbMnO_3}$ (Refs. 1 and 2) and $R\mathrm{Mn_2O_5}$,[3] for which the ferroelectric transition coincides with the transition to a complex antiferromagnetic ordered phase at low temperature. These systems are classified as *improper* ferroelectrics since the primary order parameter is the magnetization, and their electrical polarization is at least an order of magnitude lower than in proper ferroelectrics.[4] Nonetheless, the coupling between the magnetization and the electrical polarization is strong, providing an exciting playground in which to study the microscopic mechanisms that govern the magnetoelectric interaction. Moreover, the aforementioned systems commonly present a high degree of magnetic frustration, which seems closely linked to the appearance of ferroelectricity.[5]

The nature of the low-temperature state in these materials has been investigated by a variety of experimental techniques sensitive to small ionic displacements in a crystal (Raman, IR spectroscopy)[6,7] and scattering techniques sensitive to the magnetic order (neutron, resonant x-ray scattering).[8–12] An increasing number of theoretical models have also appeared over the last two years that discuss the origin of the magnetoelectric coupling.[3,13–16] Two microscopic mechanisms have been put forward: on one hand, the antisymmetric *inverse* Dzyaloshinskii-Moriya (DM) interaction, requiring a noncollinear magnetic arrangement, and on the other hand, exchange striction due to symmetric exchange. In the DM model, the polarization direction **P** (atomic displacement direction) is given by the expression

$$P \propto e_{12} \times (S_1 \times S_2), \tag{1}$$

where S_1 and S_2 are the neighboring spins and e_{12} is the propagation direction. The proportionality constant is related to the strength of the spin-orbit coupling. It seems that this mechanism explains the origin of ferroelectricity in many systems recently investigated, such as $\mathrm{TbMnO_3}$.[3,14,15] Exchange striction, which is intrinsically stronger than DM, does not require noncollinearity and has been proposed to explain the appearance of ferroelectricity in $R\mathrm{Mn_2O_5}$ (Ref. 16) and in the *E* phase of $\mathrm{HoMnO_3}$.[17] Recent work by infrared absorption confirmed that both mechanisms described above are relevant, as suggested by different polarization selection rules for the electromagnons in $R\mathrm{MnO_3}$ and $R\mathrm{Mn_2O_5}$.[18] It is important to note that due to the extremely small shifts of atoms in the ferroelectric state with respect to their positions in the centrosymmetric paraelectric phase, these displacement patterns have not yet been properly determined. The mechanism which drives the ferroelectric transition can therefore often be more easily inferred from analysis of the magnetic configuration derived from neutron diffraction experiments.

There has been continuing interest in the complex magnetic structures of $R\mathrm{Mn_2O_5}$ with R=rare earth (space group *Pbam*) since the 1960s.[19–21] These insulators order antiferromagnetically at low temperature ($T_N \approx 40$ K) with a propagation vector $(k_x,0,k_z)$ and on further cooling undergo a series of magnetic transitions to both commensurate and incommensurate magnetic phases. These materials become ferroelectric at a temperature slightly below the Néel transi-

tion at T_N with values of electric polarization ranging from 20 to 100 nC cm^{-2} depending on the R ion, being largest in the commensurate phase. The component of the magnetic propagation vector along c (k_z) depends on the size of the R cation, which suggests that the magnetic exchange along the c direction is extremely sensitive to the interlayer coupling.[9,22] Bi with r_I=131 pm has the largest ionic radius of the series and in $BiMn_2O_5$ k_z=1/2, whereas k_z=1/4 for YMn_2O_5, $HoMn_2O_5$, and $TbMn_2O_5$ with r_I=116, 116, and 118 pm, respectively.[32] On the other hand, the onset and strength of ferroelectricity does not seem to be dependent on r_I.

The magnetic structures of this class of materials have mostly been derived from neutron diffraction on polycrystalline samples. Recently, however, results obtained by single-crystal neutron diffraction for the commensurate magnetic phase of YMn_2O_5, $HoMn_2O_5$, and $ErMn_2O_5$ (Refs. 8 and 23) have been reported. The analysis suggested the presence of a small c-axis component of magnetic moment on the Mn sites, which had not been detected in previous powder measurements.[16] This additional component is in phase quadrature with the major a-b component and introduces a cycloidal modulation of the magnetic moments which could, in principle, induce ferroelectric order through the DM interaction.

In the light of this recent work, we have undertaken determination of the commensurate magnetic structures of three compounds $BiMn_2O_5$, YMn_2O_5, and $HoMn_2O_5$ using single-crystal neutron diffraction. Variation of the cations allows a comparative study, in which their influence on various characteristics of the magnetic structures can be distinguished. The aim of the study is twofold: first to systematically search for the presence of the c-axis modulation in several members of the series so as to gauge its importance in promoting ferroelectricity. Determination of the magnitude of this component for all three compounds is especially important because the magnetic propagation vector in $BiMn_2O_5$ ($k_z=\frac{1}{2}$) differs from that in $HoMn_2O_5$ and YMn_2O_5 ($k_z=\frac{1}{4}$). Second, by studying $HoMn_2O_5$, we can investigate the influence of a magnetic R ion on the arrangement of the Mn moments and determine the magnetic ordering of the Ho sublattice itself. A comparison with YMn_2O_5, which has the same propagation vector but a nonmagnetic R site, is of particular interest, since the values of the electric polarization in the commensurate regime of the two systems are significantly different.

II. EXPERIMENT

Single crystals of RMn_2O_5 (R=Bi, Y, and Ho) were grown using $B_2O_3/PbO/PbF_2$ flux in a Pt crucible. The flux was held at 1280 °C for 15 h and slowly cooled down to 950 °C at a rate of 1 °C/h. Crystals grew in the form of cubes. The samples used for the present work were respectively of sizes: $\sim 4\times4\times4$ mm^3 for YMn_2O_5, $1\times1\times3$ mm^3 for $HoMn_2O_5$, and $2\times2\times2$ mm^3 for $BiMn_2O_5$, where the three dimensions refer to the [110], [$\bar{1}$10], and [001] directions. For the $HoMn_2O_5$ crystal, additional faces (100) and (010) were also visible. Single-crystal diffraction measurements were performed on the four-circle diffractometer D10 at the ILL (Grenoble, France). Samples were checked for quality and prealigned with the (001) direction oriented along the vertical axis by using the OrientExpress facility (ILL). Samples were mounted on standard aluminum pins in a He exchange gas cryostat. Data were collected with an incident neutron wavelength of λ=2.36 Å by using an 80 mm^2 two-dimensional microstrip detector. Ω scans around each Bragg reflection were performed, with variable counting time depending on the intensity. Peak integration was performed using the program RACER (ILL) in two steps. First, a library was built by fitting ellipsoidal shapes to a set of strong reflections ($I>3\sigma$), these shapes were used in a second pass to integrate all reflections. Data were collected for all three samples in the ordered magnetic commensurate phases. An additional data set was collected for the YMn_2O_5 sample in the low-temperature incommensurate phase, but the results will be reported elsewhere. The data sets for YMn_2O_5 were collected at T=25 K (nuclear and magnetic scattering), those for $BiMn_2O_5$ at T=10 K (nuclear and magnetic scattering) and for $HoMn_2O_5$ at T=50 K (nuclear scattering), and T=25 K (magnetic scattering). For each data set, the list of integrated intensities obtained were corrected for Lorentz factors and normalized to an arbitrary monitor count. Determination of both the nuclear and magnetic structures were carried out using the FULLPROF program suite.[24] For each sample, the following procedure was applied: the published crystallographic models, space group *Pbam*, were used to refine the nuclear data sets. Because a limited Q range is accessible on D10, the crystallographic parameters were fixed, with the exception of a global thermal parameter to account for different temperatures. In addition, a global scale factor was refined together with six parameters for extinction correction, following the formulation of Becker-Coppens for anisotropic extinction (extinction model number 4 in FULLPROF). This correction is particularly important for YMn_2O_5 because of the large size of the crystal. The scale factors that are obtained by refining the nuclear structure were used and fixed for refinement of the magnetic structures.

III. RESULTS

A. Crystal structure and formalism

The crystal structure and topology of the magnetic interactions have been described in detail in Refs. 16 and 25. The different atomic positions for Mn^{3+} and Mn^{4+} (and Ho^{3+}) have been numbered according to Ref. 25. To facilitate the identification of all magnetic sites in the figures, additional labels have been included: a for Mn^{3+} and b for Mn^{4+} (c for Ho^{3+}). The crystal structure of RMn_2O_5 (isostructural throughout the series) is displayed in Fig. 1 and the correspondence between labels and atomic positions can be found in Table I. Mn^{3+} (a) is five coordinated by oxygen ions, in square-pyramid geometry, while Mn^{4+} (b) is six coordinated in distorted octahedral geometry. There are four symmetry equivalent Mn^{3+} sites and four Mn^{4+} sites per unit cell. The pyramids centered at a2 and a3 (also a1 and a4) share an edge of their basal plane. All Mn^{3+} are located on a mirror

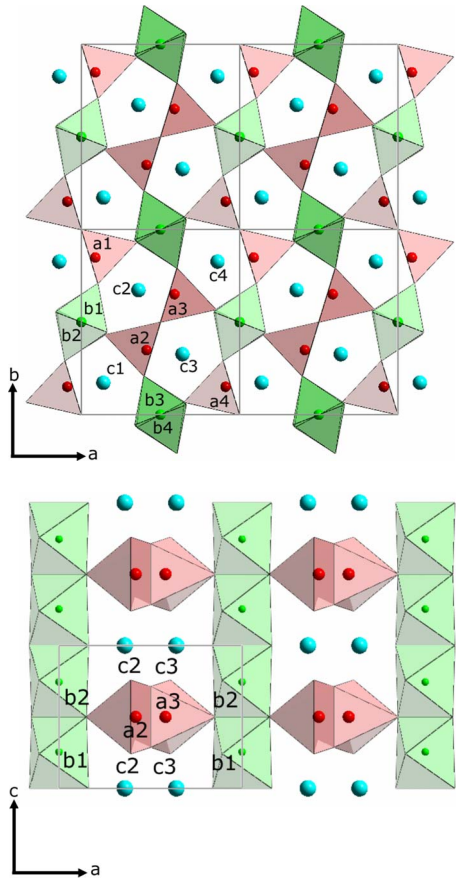

FIG. 1. (Color online) Crystal structure of RMn_2O_5 projected in the *ab* plane (top panel) and *ac* plane (bottom panel). The green (small and light gray), red (gray), and blue (black) spheres correspond to Mn^{4+}, Mn^{3+}, and R^{3+} ions, respectively. Mn-O polyhedra are shown with the same color scheme. The thin black line represents the crystallographic unit cell. Correspondence between the labels and atomic positions are described in Table I.

plane at $z=0.5$. The octahedra coordinating the Mn^{4+} sites b1 and b2 (also b3 and b4) share edges to form chains running along the *c* direction. The b1 (b3) atoms with $z\sim0.25$ and b2 (b4) with $(1-z)\sim0.75$ lie below and above the Mn^{3+} layer. It should be noted that the sites b1 and b2, also b3 and b4, are related by a center of symmetry. The Mn^{4+} octahedra share corners with $Mn^{3+}O_5$ pyramids to form layers in the *ab* plane. The *R* ions (labeled c for $HoMn_2O_5$) occupy the $(x,y,0)$ site, of multiplicity four, and are all positioned in the $z=0$ layer separating two Mn^{3+}/Mn^{4+} layers.

The magnetic structures have been analyzed by using the propagation-vector formalism, in which magnetic moments for all sites described above are expanded in Fourier series. We briefly describe the conventions used in the next paragraph. For a magnetic structure with a single propagation vector $\vec{k}$, which is the relevant case in this study, a magnetic moment of atom type *j* in the crystallographic unit cell l ($\overrightarrow{m_{lj}}$) is written as

$$\overrightarrow{m_{lj}} = \sum_k \overrightarrow{S_{kj}} \cdot e^{-2\pi \cdot i \cdot (\vec{k} \cdot \vec{R_l} + \phi_j)}, \tag{2}$$

where the sum runs over $\vec{k}$ and $-\vec{k}$ if these vectors are not related by a reciprocal lattice vector (case of YMn_2O_5 and $HoMn_2O_5$) or uniquely $\vec{k}$ otherwise (case of $BiMn_2O_5$). $\vec{R_l}$ is a pure lattice translation and ϕ_j is a phase factor. The magnetic structure is fully determined by giving a set of Fourier coefficients and phases $(\overrightarrow{S_{kj}}, \phi_j)$ for each *j*, i.e., seven components per site in the most general case since the Fourier coefficients are complex quantities. We note that because $\overrightarrow{m_{lj}}$ is a real quantity, the constraint $\overrightarrow{S_{-kj}} = \overrightarrow{S^*_{kj}}$ (where * denotes the complex conjugate) is required. It is important to mention that ϕ_j are relative phases and are equal for sites belonging to the same orbit, i.e., sites that can be transformed into each other by an operation of the magnetic little group. It is

TABLE I. Magnetic Fourier coefficients obtained from least-squares refinements of the single crystal diffraction data for $HoMn_2O_5$ at $T=25$ K (see text for details). The Fourier coefficients for each site in the primitive unit cell are given along crystallographic direction (x,y,z) and labeled *M* and *I* when real and imaginary, respectively. The phase for each site (Ph) is given in units of 2π. The error bars are given for all parameters within parentheses.

Label	Atom	Position	M_x	M_y	I_z	Ph
b1	Mn^{4+}	(0 0.5 0.2558)	−2.25(4)	0.58(5)	−0.38(8)	0.088(2)
b2	Mn^{4+}	(0 0.5 0.7442)	−2.32(4)	0.59(5)	−0.39(8)	0.161(2)
b3	Mn^{4+}	(0.5 0 0.2558)	2.26(4)	0.59(5)	−0.51(8)	0.088(2)
b4	Mn^{4+}	(0.5 0 0.7442)	2.19(4)	0.55(5)	−0.49(8)	0.161(2)
a1	Mn^{3+}	(0.0885 0.849 0.5)	−3.53(4)	−0.43(5)	0.58(9)	0.125
a2	Mn^{3+}	(0.4115 0.349 0.5)	3.49(4)	−0.73(5)	0.46(9)	0.125
a3	Mn^{3+}	(0.5885 0.651 0.5)	−3.29(4)	0.85(6)	−0.60(8)	0.125
a4	Mn^{3+}	(0.9115 0.151 0.5)	−3.27(4)	−0.72(6)	0.65(8)	0.125
c1	Ho^{3+}	(0.1392 0.1713 0)	0.03(3)	−1.09(4)	0.18(7)	−0.001(2)
c2	Ho^{3+}	(0.3608 0.6713 0)	−0.03(3)	−1.14(4)	0.16(6)	−0.001(2)
c3	Ho^{3+}	(0.6392 0.3284 0)	−1.27(4)	−0.04(4)	−0.16(6)	−0.001(2)
c4	Ho^{3+}	(0.8606 0.8287 0)	−1.25(4)	−0.08(4)	0.24(6)	−0.001(2)

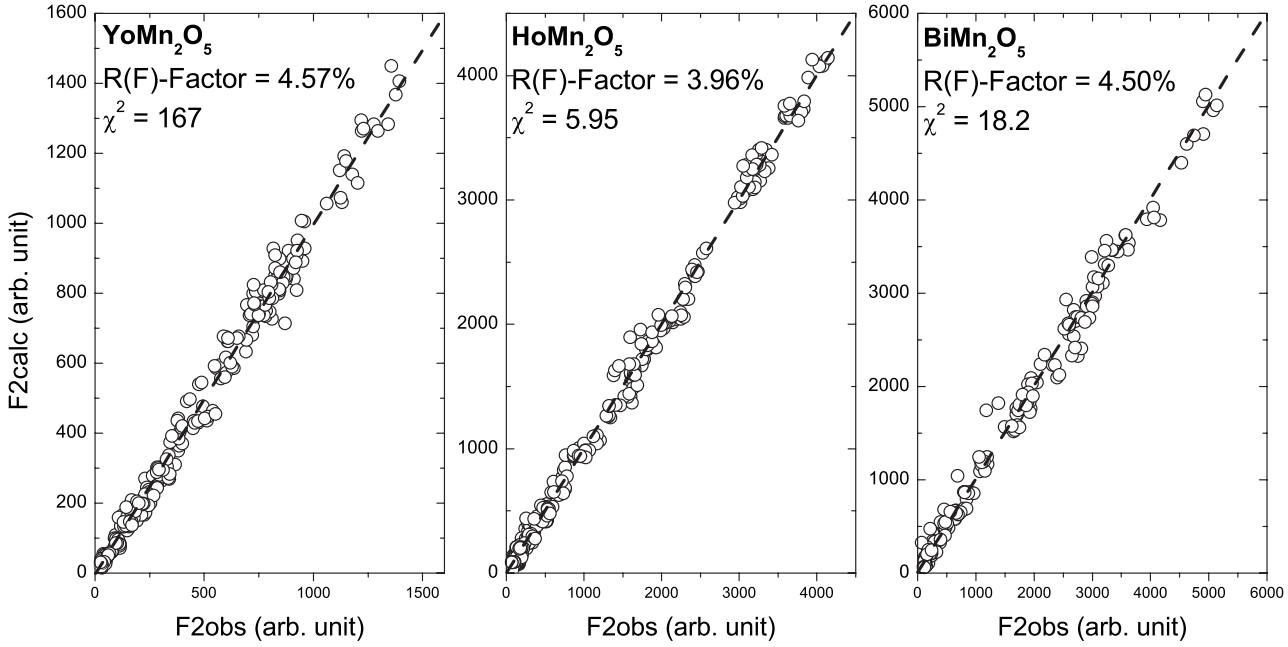

FIG. 2. Results of the refinement for the commensurate magnetic structures for three compounds YMn_2O_5, $HoMn_2O_5$, and $BiMn_2O_5$. The experimental structure factors (times a scale factor) are plotted against the calculated ones. The agreement factors–magnetic $R(F)$ factors and χ^2 are shown. See text for details of the magnetic models.

different to a global phase, which simultaneously applies to all magnetic sites and rephases the entire magnetic structure. Such a phase cannot be determined by diffraction since the integrated intensities are proportional to the norm of the magnetic interaction vector. Additional constraints exist between $(\vec{S_{kj}}, \phi_j)$ of symmetry-related sites. These constraints are determined by representation analysis and will be briefly described in the following sections based on previously published work.[26]

B. YMn_2O_5

1. Magnetic structure

The propagation vector for the Y compound in the commensurate phase is $\vec{k}=(1/2,0,1/4)$. Symmetry analysis[26] indicates that the Mn^{4+} sites are split into two orbits because the m_z mirror-plane operation does not belong to the little group. The first and second orbits contain, respectively, the b1/b3 sites and b2/b4 sites. The ϕ_j phases for each orbit can therefore be nonequal and treated as free parameters during the refinement. On the other hand, the phases of the Mn^{3+} sites, belonging to a single orbit, must be equal. We arbitrarily chose to fix the phase of the Mn^{3+} sites at 0.125 (one phase must be fixed since structure factors do not depend on a global phase) for comparison with results reported earlier from powder data,[16] describing a configuration with equal moments. In this case, representation analysis does not impose any constraints on the magnitude and direction of the Fourier coefficients for both Mn^{3+} and Mn^{4+} sites.[26] For each site, six independent Fourier coefficients are in principle refinable. The unconstrained model has therefore 50 parameters and describes the most general magnetic structure. For typical magnetic structures that are described by either spin-density waves (SDW) or simple cycloidal modulations, some of these parameters will be fully correlated. Refining an unconstrained model against the 355 independent magnetic reflections fails due to the large number of parameters and the presence of strong correlations. In order to find possible models, a global optimization algorithm, using the simulated annealing procedure described in Ref. 27, was employed. Systematically, the Fourier coefficients for all magnetic sites were found to be principally along the a axis, whether real or imaginary. In addition, a weaker b-axis component was found with the same character (real or imaginary) as the a component. These two components define a vector, say, v_1 in the ab plane. A small c-axis component in phase quadrature with the a and b components was also identified. The structure therefore has a small helicoidal modulation, with rotation axis given by the cross product of v_1 with a vector along z. A model with this configuration, i.e., one in which the Fourier coefficients for all magnetic sites are real in the ab plane and imaginary along c, has been constructed; it has 26 refinable parameters. The lower number of free parameters allowed a direct least-squares refinement to be made which converged after a few cycles. The structure factors that are calculated with this model are shown, plotted against those observed, in Fig. 2. The model was found to reproduce the observed data very well with a magnetic $R(F)$ factor[33] of 4.57% (Fig. 2). For this particular sample, the large value of $\chi^2=163$ is explained by high statistics of the data obtained on a large sample with long counting time. The refined values of the Fourier coefficients are displayed in Table II and the magnetic structure projected along two different crystallographic directions in Figs. 3 and 4. The magnetic arrangement in the ab plane (Fig. 3) is equivalent to that derived in our previous work from powder data.[16] The moment directions are within $\sim 10°$ of the a axis for Mn^{3+} and $\sim 14°$ for

TABLE II. Magnetic Fourier coefficients obtained from least-square refinements of the single crystal diffraction data for YMn_2O_5 at $T=25$ K (see text for details). The Fourier coefficients for each site in the primitive unit cell are given along crystallographic direction (x,y,z) and labeled M and I when real and imaginary, respectively. The phase for each site (Ph) is given in units of 2π. The error bars are given for all parameters within parentheses.

Label	Atom	Position	M_x	M_y	I_z	Ph
b1	Mn^{4+}	(0 0.5 0.25513)	2.01(5)	−0.47(8)	0.36(11)	0.095(2)
b2	Mn^{4+}	(0 0.5 0.74487)	2.13(5)	−0.53(9)	0.44(11)	0.156(2)
b3	Mn^{4+}	(0.5 0 0.25513)	−2.07(5)	−0.53(8)	0.4(1)	0.095(2)
b4	Mn^{4+}	(0.5 0 0.74487)	−1.99(5)	−0.51(8)	0.45(11)	0.156(2)
a1	Mn^{3+}	(0.08805 0.85079 0.5)	3.16(6)	0.59(9)	−0.46(12)	0.125
a2	Mn^{3+}	(0.41195 0.35079 0.5)	−3.18(6)	0.55(9)	−0.50(12)	0.125
a3	Mn^{3+}	(0.58805 0.64921 0.5)	3.01(5)	−0.67(9)	0.56(13)	0.125
a4	Mn^{3+}	(0.91195 0.14921 0.5)	2.99(5)	0.65(9)	−0.60(13)	0.125

Mn^{4+}, defining zigzag antiferromagnetic (AFM) chains running along a. One of these chains links b1, b2, a2, and a3, and the other links b3, b4, a4, and a1. In addition, there is a significant c component on all magnetic sites, as suggested by Noda *et al.*,[8] which was not found in our earlier analysis of powder data. The c components have almost the same magnitude as the b components on both Mn sites. Their imaginary character means that the modulation is in quadrature with the real *in-plane* components. This can be seen in Fig. 4; for example, for the a2 site, the in-plane components of the magnetic moment follow a $(-++-)$ sequence across four unit cells along c, while the c component follows a $(--++)$ sequence. This result is also in agreement with the work of Noda *et al.*[8]

The refined values of the phases for sites b1/b3 and b2/b4, respectively, 0.095(2) and 0.156(2), are slightly different from the fixed values of 0.125 used for fitting powder data. Consequently, and in addition to the existence of a c component, the magnetic moments on sites b1 and b2 (as well as b3 and b4) are of different magnitudes, as shown in Fig. 4. We also note that there is a symmetric deviation of these phases with respect to Mn^{3+} phase of 0.125 $[(0.125-\delta)$ for the first orbit and $(0.125+\delta)$ for the second orbit]. The identification of a small c component has direct implications on the nature of the magnetic configuration, previously described as a pure SDW: small cycloidal modulations propagating along the edge-sharing $Mn^{4+}O_6$ chains are observed in the ac and bc planes (Fig. 5). In the ac plane, the moment rotation direction is clockwise for Mn^{4+} chains formed by the b1 and b2 sites (left panel of Fig. 4) and anticlockwise for chains formed by the b3 and b4 sites (right panel of Fig. 4). In the bc plane, the weak cycloidal modulation, as highlighted in Fig. 5, rotates in the same direction along the b1/b2 chains and b3/b4 chains. The Mn^{3+} moments are also slightly tilted along the c direction, remaining almost collinear to adjacent Mn^{4+} magnetic moments in a given AFM chain. Therefore, the presence of antiferromagnetic chains running along the a axis, identified earlier as an important characteristic of these systems, remains valid despite the small c component.

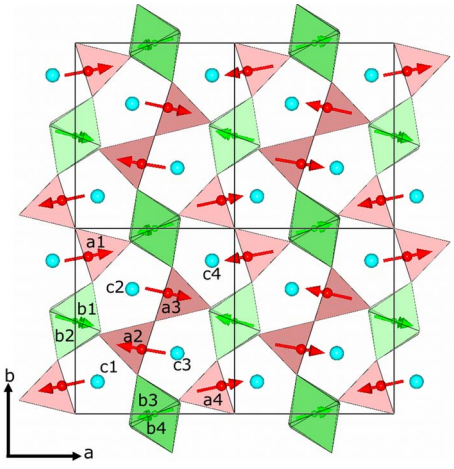

FIG. 3. (Color online) Magnetic structure of YMn_2O_5 projected in the ab plane. The structure is shown in two unit cells, marked by thin black lines, along the a and b axes. The green (small and light gray) and red (gray) arrows represent magnetic moments on Mn^{4+} and Mn^{3+} sites, respectively. Corresponding Mn-O polyhedra are shown with the same colors. The blue spheres (black) represent Y ions. The different sites are labeled according to Table II.

2. Domains

The arm of the star of k is made only of the two vectors $\vec{k}=(\frac{1}{2},0,\frac{1}{4})$ and $-\vec{k}$ since the vectors $(-\frac{1}{2},0,\frac{1}{4})$ and $(\frac{1}{2},0,-\frac{1}{4})$ are related to k and $-k$ by a reciprocal lattice vector. Therefore, a single k domain contributes to the scattering. On the other hand, one must take into account the "orientation" domains, i.e., domains that are obtained by applying symmetry operations of the paramagnetic group that are not valid operations (lost) of the magnetic structure. Four symmetry operations of the paramagnetic group (combined or not with complex conjugation) leave the magnetic structure unchanged, as shown in Table III. We refer to this domain as domain one (D1). The other four symmetry operations all transform the magnetic structure described in the previous section into an inequivalent one (domain 2, D2, as shown in Fig. 6). No other domains exist, and D1 and D2 are simply related by inversion symmetry. Inversion symmetry differently operates on different magnetic sites: for b_3, b_4, a_1, and a_4, belonging to one of the zigzag AFM chains, the applica-

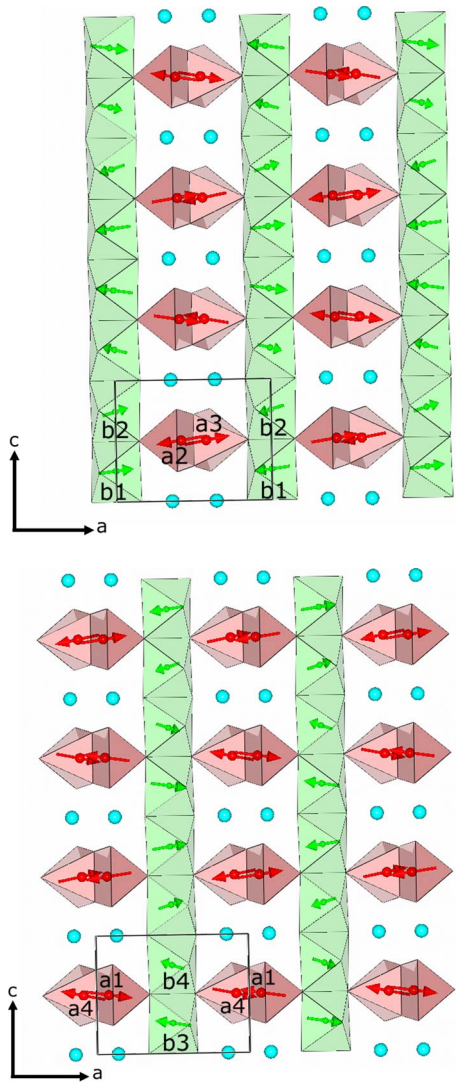

FIG. 4. (Color online) Magnetic structure of YMn_2O_5 projected in the *ac* plane shown within four unit cells along *c* and two unit cells along *a*. The projection is separately shown for magnetic sites belonging to the first AFM chain (top) and the second chain (bottom) (see text for details). The green (small and light gray) and red (gray) arrows represent magnetic moments on Mn^{4+} and Mn^{3+} sites, respectively. Corresponding Mn-O polyhedra are shown with the same colors. The blue (black) spheres represent Y ions. The different sites are labeled according to Table II.

tion of inversion symmetry leaves the *a* and *b* moment components unchanged, while it changes the sign of the *c* component. In contrast for sites b_1, b_2, a_2, and a_3 (the other AFM chain), inversion symmetry reverses the sign of the *a* and *b* components while preserving the *c* component. Since D1 and D2 are related by inversion symmetry, the diffracted intensities arising from both domains are identical for a nonpolarized diffraction experiment and refining the data assuming any domain leads to the same result. We note that the two domains are also related by a simple rotation by 180° along the *z* axis or the *x* axis.

From the list of symmetry operations (Table III) that leave the magnetic structure invariant (modulo complex conjugation operation), one derives the point group *m*2*m* in the magnetically ordered phase, which is in agreement with that obtained earlier from corepresentation analysis.[26] This point group is compatible with ferroelectricity along the *b* axis, irrespective of the microscopic magnetoelectric mechanism.

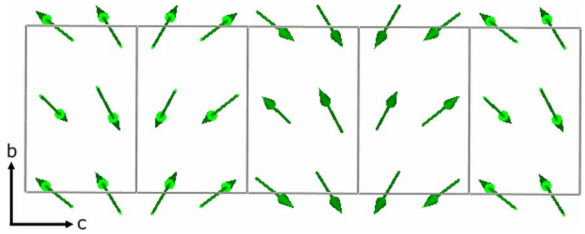

FIG. 5. (Color online) Magnetic structure of YMn_2O_5 projected in the *bc* plane and showing only the Mn^{4+} moments. The figure shows the small helicoidal modulation generated by the out-of-phase *c* component. To highlight this weak modulation, the moments have been scaled by a factor of 5 with respect to what represented in the other figures.

C. $HoMn_2O_5$

$HoMn_2O_5$ orders AFM at $T=44$ K first with an incommensurate propagation vector $\vec{k}=(0.48,0,0.245)$, followed by a lock in at $T=38$ K to a commensurate $\vec{k}=(\frac{1}{2},0,\frac{1}{4})$. The magnetic structure has been determined in the commensurate phase from 381 independent magnetic reflections by using the same procedure as that described in the case of YMn_2O_5. However, in this case, the magnetic ordering of Ho is an additional complexity, which increases the number of free parameters. Attempting to refine the data without a magnetic contribution on the Ho sites leads to poor agreement factors $[R(F)=20.2\%]$, as already reported from analyzing powder diffraction patterns.[25] Preliminary measurements with resonant x-ray scattering at the L_{III} edge directly confirm the magnetic ordering of Ho. Symmetry analysis indicates that the four equivalent Ho positions belong to the same orbit and therefore only one phase parameter is required. However, there are no constraints between components of the moment of different sites, which were independently refined. The fi-

TABLE III. Action of the symmetry operations of the paramagnetic group on the magnetic structure of domain 1. Domain one and two are abbreviated by D1 and D2. Symmetry operations are shown in the Seitz notation. The $*$ symbol indicates combination of the symmetry operation with complex conjugation operation.

Symmetry operation	Domain generated
$\{1\|000\}$	D1
$\{\bar{1}\|000\}^*$	D2
$\{m_{xy0}\|000\}^*$	D1
$\{2_z\|000\}$	D2
$\{m_{0yz}\|0\frac{1}{2}0\}$	D1
$\{m_{x0z}\|\frac{1}{2}00\}$	D2
$\{2_{x00}\|\frac{1}{2}00\}^*$	D2
$\{2_{0y0}\|0\frac{1}{2}0\}^*$	D1

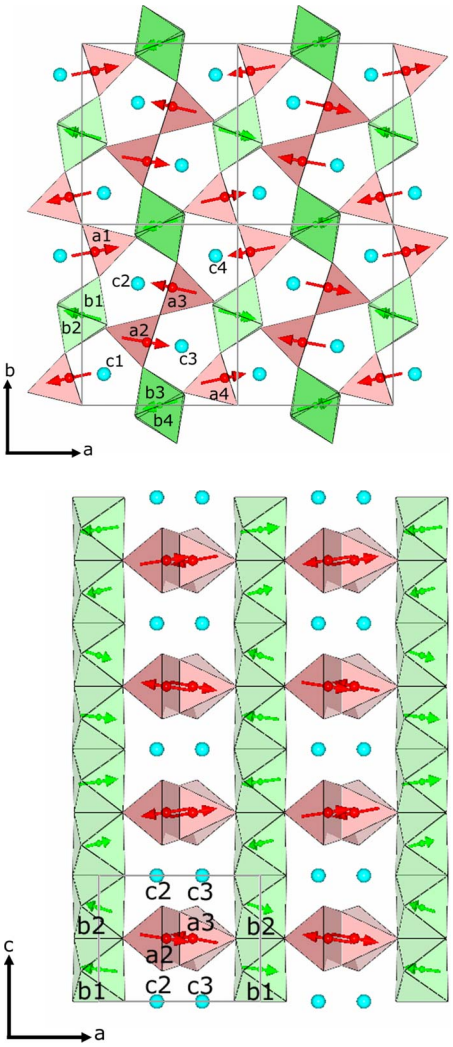

FIG. 6. (Color online) Magnetic structure of YMn_2O_5 projected in the *ab* plane (top panel) and the *ac* plane (bottom panel) for the second domain, obtained by applying inversion symmetry on the magnetic structure of the first domain (Figs. 3 and 4).

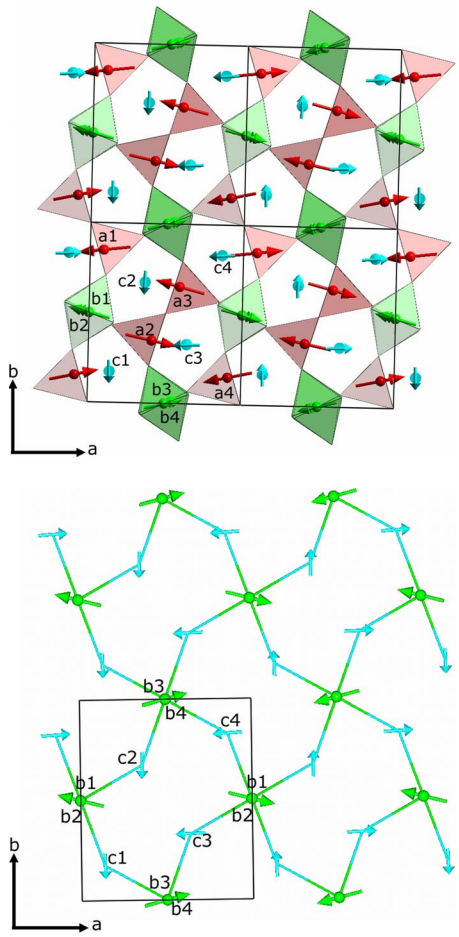

FIG. 7. (Color online) Magnetic structure of $HoMn_2O_5$ projected in the *ab* plane. The structure is shown in two unit cells, marked by thin black lines, along the *a* and *b* axes. The green (small and light gray), red (gray), and blue (black) arrows (top panel) represent magnetic moments on Mn^{4+}, Mn^{3+}, and Ho^{3+} sites, respectively. Corresponding Mn-O polyhedra are shown with the same colors. For clarity, in the bottom panel only Mn^{4+} and Ho^{3+} (belonging to an ordered Ho layer) magnetic moments are shown, respectively, in green (small and light gray) and blue (black) color. The lines connecting Mn^{4+} and Ho^{3+} represent interactions (see text for details). The different sites are labeled according to Table I.

nal refinement contained 45 parameters and was found to reproduce the data very well with structure factor $R(F)=3.96\%$ and $\chi^2=5.82$. The magnetic structure is similar to the model recently proposed by Kimura *et al.*[23] and to the YMn_2O_5 one, with the appearance of almost collinear $\cdots$-Mn^{4+}-Mn^{3+}-Mn^{3+}-Mn^{4+}-$\cdots$ AFM zigzag chains in the *ab* plane. These chains make an angle of $\sim 14°$ with respect to the *a* axis. We again found a small *c* component (Fig. 8) of moment on all Mn magnetic sites, in quadrature with the in-plane components and of magnitude similar to that observed for YMn_2O_5. The refined phase for the Ho sites is shifted by 0.126(2) with respect to the Mn^{3+} sites. The Ho moments at the c3/c4 sites are parallel to the *a* axis and those at the c1/c2 sites to the *b* axis (Fig. 7 and Table I). It is possible that a smaller $\pi/2$ out-of-phase component along *c* may exist, but the refined magnitudes are only three times larger than the error bars. Although the magnetic configuration of the Ho sites is identical to that derived earlier by simulated annealing using powder data,[25] the orientation of the Ho moments in the *ab* plane is quite different. The values of the Ho moments, ranging from $1.1\mu_B$ to $1.3\mu_B$, are much smaller than the fully saturated value for a $J=8$ state. This can be partly explained by splitting of the fully degenerate $J=8$ state by the crystal field, but typical crystal-field energies in oxides will lead to a moment much larger than observed here.[28] Additional reduction can be due thermal excitation, at 25 K, of levels above the ground state (Ho^{3+} is a non-Kramer ion characterized by singlet levels). We argue that the Ho moment of $\sim 1.1\mu_B$ in $HoMn_2O_5$ is mainly due to superexchange interactions via the 2*p* oxygen orbitals. Exactly half of the Ho layers show ordered magnetic moments in the *ab* plane, while the other half show only a small moment along the *c* direction (Fig. 8). Accordingly, in the former type of layers, we can clearly show that the directions of the moment are systematically arranged along the resultant of AFM superexchange interactions with the four nearest-neighbor Mn^{4+} sites (Figs. 7 and 8). The net moment

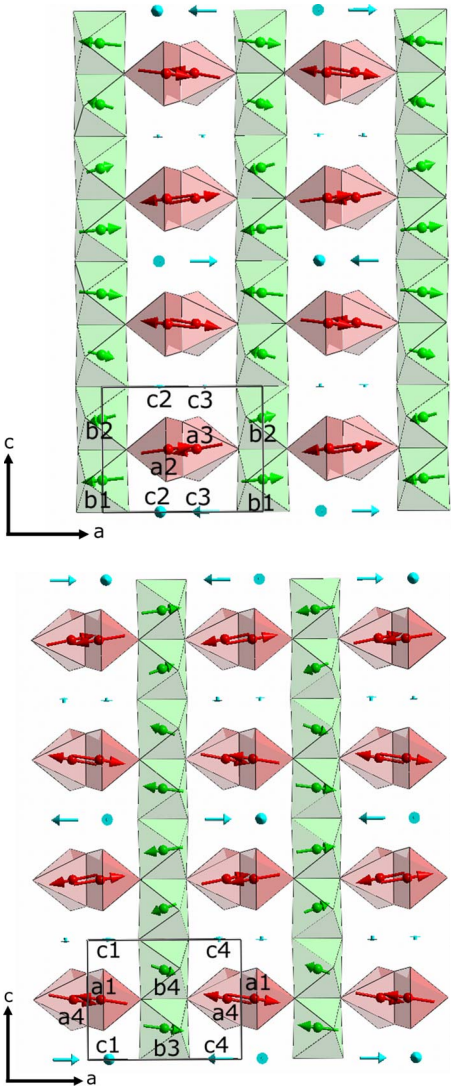

FIG. 8. (Color online) Magnetic structure of $HoMn_2O_5$ projected in the *ac* plane shown within four unit cells along *c* and two unit cells along *a*. The projection is separately shown for magnetic sites belonging to the first AFM chain (top) and the second chain (bottom) (see text for details). The green (small and light gray), red (gray), and blue (black) arrows represent magnetic moments on Mn^{4+}, Mn^{3+}, and Ho^{3+} sites, respectively. Corresponding Mn-O polyhedra are shown with the same colors. The different sites are labeled according to Table I.

on each Ho site is pointing either along the *a* axis (sites c3 and c4) or *b* axis (sites c1 and c2), resulting from the cancellation of, respectively, the *b* and *a* components of neighbor Mn^{4+} moments. Also, the resultant of the superexchange is larger for sites c3 and c4 (along the *a* direction) than for sites c1 and c2 (along *b*), which should lead to different Ho moments on these sites, as we appear to experimentally observe (Table I). A more precise determination of the respective magnitude of the moments on sites c1/c2 and c3/c4 is currently underway by resonant x-ray scattering. Calculations show that azimuthal scans on magnetic Bragg peaks at the Ho L_{III} edge are extremely sensitive to these parameters (as well as being Ho selective).

The magnetic configuration of the Ho sublattice also breaks inversion symmetry since moments on sites c2 and c3 (respectively, c1 and c4) are pointing in different directions. As in the case of YMn_2O_5, there are only two orientation domains to consider, related by inversion symmetry and therefore contributing equally to the diffracted intensities. The symmetry operations and corresponding domains listed in Table III are also valid for $HoMn_2O_5$. The magnetic structure of domain 2 including the transformed Ho moments (not shown) is easily derived from domain 1 by applying inversion symmetry. In this case, the magnetic point group is also *m*2*m*, which supports ferroelectricity along the *b* axis.

D. $BiMn_2O_5$

$BiMn_2O_5$ is the only member of the series that shows magnetic ordering below $T=39$ K with a propagation vector $\vec{k}=(\frac{1}{2},0,\frac{1}{2})$ and no transitions to incommensurate magnetic order. Because of the commensurate propagation vector representation analysis leads to stricter constraints than those applicable to YMn_2O_5 and $HoMn_2O_5$, they are described in detail by Muñoz *et al.*[22] No phases are required at any of the sites since $\vec{k}$ is half a reciprocal lattice vector. The magnetic representation contains two irreducible representations of dimension 2. Only magnetic modes belonging to the representation Γ_1 fit our single crystal data, in agreement with the results of Muñoz *et al.*[22] The magnetic moments on Mn^{4+} sites are constrained in the following way: sites b1 and b2 have the same *a* and *b* components but opposite *c* components. The same relation holds for sites b3 and b4. However, there are no relationships imposed by symmetry between the two sets of sites mentioned above, b1/b2 on one hand and b3/b4 on the other. For the Mn^{3+} sites, the moments are constrained to lie in the *ab* plane but can have any magnitude and orientation within it. In the work of Muñoz *et al.*,[22] the additional physical constraint of equal moments, not imposed by symmetry, was introduced. Here, the large number of independent magnetic reflections collected (204) allows the simultaneous refinement of all 14 parameters. The result of the refinement is shown in Fig. 2 and the corresponding magnetic structure is displayed in Figs. 9 and 10 (cf. Table IV). A $R(F)$ factor of 4.5% has been obtained with a χ^2 value of 18.2. $BiMn_2O_5$ has a very similar magnetic structure to that previously described for YMn_2O_5, for instance, the antiferromagnetic $\cdots$-Mn^{4+}-Mn^{3+}-Mn^{3+}-Mn^{4+}-$\cdots$ chains in the *ab* plane. This is at variance with the structure proposed by Muñoz *et al.*,[22] in which there is a noncollinear arrangement of Mn^{4+} and Mn^{3+} moments within one AFM chain. The angular deviation of the AFM chains from the *a* axis ($\sim 8°$) is less pronounced than in the YMn_2O_5 and $HoMn_2O_5$ compounds. Also, unlike YMn_2O_5 and $HoMn_2O_5$, we found a much smaller *z* component for the Mn^{4+} moments. The magnetic point group is *m*2*m* and the magnetic structures of the two possible domains are related by inversion symmetry, as previously described, resulting in flipping the central AFM chain in Fig. 9.

IV. ORIGIN OF FERROELECTRICITY

In this section, we discuss the possible mechanism that will promote a ferroelectric state in the magnetically ordered

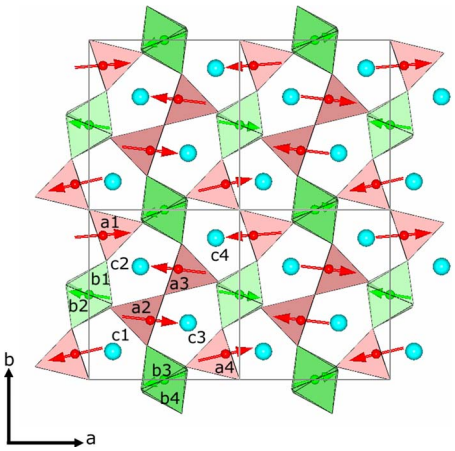

FIG. 9. (Color online) Magnetic structure of $BiMn_2O_5$ projected in the *ab* plane. The structure is shown in two unit cells, marked by thin black lines, along the *a* and *b* axes. The green (small and light gray) and red (gray) arrows represent magnetic moments on Mn^{4+} and Mn^{3+} sites, respectively. Corresponding Mn-O polyhedra are shown with the same colors. The blue (black) spheres represent Bi ions. The different sites are labeled according to Table IV.

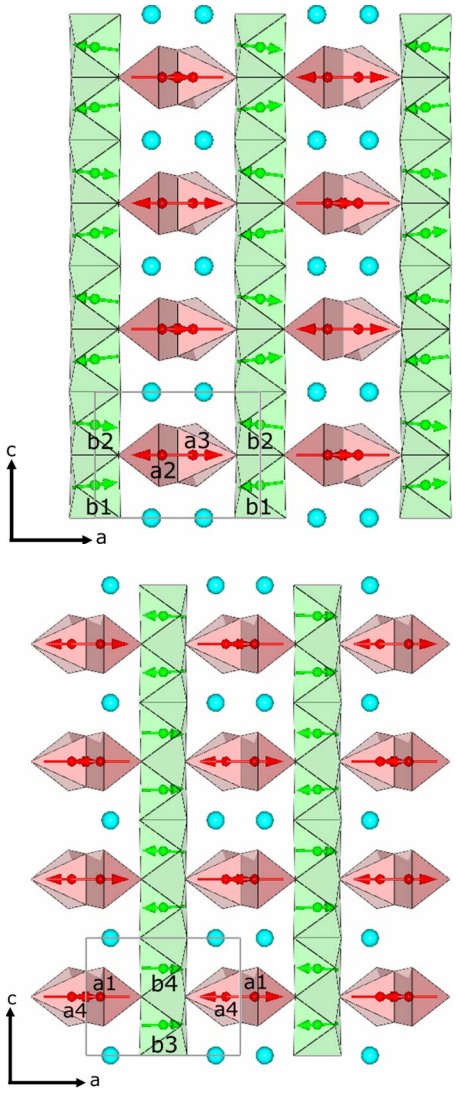

FIG. 10. (Color online) Magnetic structure of $BiMn_2O_5$ projected in the *ac* plane shown within four unit cells along *c* and two unit cells along *a*. The projection is separately shown for magnetic sites belonging to the first AFM chain (top) and the second chain (bottom) (see text for details). The green (small and light gray) and red (gray) arrows represent magnetic moments on Mn^{4+} and Mn^{3+} sites, respectively. Corresponding Mn-O polyhedra are shown with the same colors. The blue (black) spheres represent Bi ions. The different sites are labeled according to Table IV.

phase. First of all, it is worth noting that irrespective of the microscopic mechanism involved, the point group symmetry *m*2*m* derived from the magnetic structures of YMn_2O_5, $HoMn_2O_5$, and $BiMn_2O_5$, is consistent with ferroelectric order only along the *b* axis. Second, it is important to discuss the possible microscopic mechanisms, in the light of the additional weak magnetic components observed along the *c* axis for YMn_2O_5 and $HoMn_2O_5$ and not previously identified by powder diffraction. This small out-of-plane component introduces a modulation that resembles a cycloid, even though it does not correspond to a homogeneous rotation from site to site, as seen in Fig. 4, for example. However, this modulation could in principle give rise to ferroelectricity based on antisymmetric exchange interaction, a mechanism proposed in several multiferroics, and its strength will be proportional to the spin-orbit coupling, potentially large for octahedral Mn^{4+}. Obviously, the much smaller modulation in $BiMn_2O_5$, multiferroic with a value of the electrical polarization comparable to YMn_2O_5 and $HoMn_2O_5$, does not support this picture. Therefore, we argue that our model based on symmetric exchange and proposed initially in Ref. 29 is the principal mechanism driving ferroelectric order. The recent observation of electromagnons[18] active only for certain polarization directions also supports a model based on symmetric-exchange interaction. This model is relevant since the magnetic configuration in the *ab* plane for the three compounds studied here is frustrated, i.e., the magnetic energy is invariant by flipping any AFM chain in the lattice.

Such a configuration will induce atomic displacements on some of the ions in the crystal (we speculated that mainly Mn^{3+} ions are involved based on structural anomalies related to this site) that will lower the magnetic energy.[6,16,30] This comes at the cost of elastic energy, quadratic with the displacement, but for small displacements the gain in magnetic energy (linear with displacements) overcomes the elastic energy cost. Magnetostriction due to symmetric exchange should be much stronger than the DM interaction, which is a relativistic effect.[14,15,31] However, it is possible that this latter mechanism contributes to the total electric polarization in the YMn_2O_5 and $HoMn_2O_5$ compounds but should be of minor importance. In fact, the two mechanisms are likely to be strongly coupled. It is important to note that applying the inversion symmetry operation not only flips one of the AFM chains but also changes the rotation direction of the cycloidal modulation. Therefore, the direction of the electric polarization in domain two is opposite to that in domain one, whatever the mechanism considered. The observation of cycloidal structures for many of these compounds is intriguing, and is unlikely to be a coincidence. In general, two mechanisms are

TABLE IV. Magnetic Fourier coefficients obtained from least-squares refinements of the single crystal diffraction data for $BiMn_2O_5$ at $T=10$ K (see text for details). The Fourier coefficients for each site (M, real) in the primitive unit cell are given along crystallographic direction (x,y,z). The phase for each site (Ph) is given in units of 2π. The error bars are given for all parameters within parentheses.

Label	Atom	Position	M_x	M_y	M_z	Ph
b1	Mn^{4+}	(0 0.5 0.2613)	2.10(3)	−0.33(6)	0.25(6)	0.0
b2	Mn^{4+}	(0 0.5 0.7387)	2.10(3)	−0.33(6)	−0.25(6)	0.0
b3	Mn^{4+}	(0.5 0 0.2613)	2.07(3)	0.56(6)	0.08(6)	0.0
b4	Mn^{4+}	(0.5 0 0.7387)	2.07(3)	0.56(6)	−0.08(6)	0.0
a1	Mn^{3+}	(0.0926 0.8516 0.5)	−2.83(5)	−0.23(10)	0.000	0.0
a2	Mn^{3+}	(0.4074 0.3516 0.5)	−2.83(5)	0.33(10)	0.000	0.0
a3	Mn^{3+}	(0.5926 0.6484 0.5)	2.80(5)	−0.34(9)	0.000	0.0
a4	Mn^{3+}	(0.9074 0.1484 0.5)	−2.74(5)	−0.64(10)	0.000	0.0

known to generate helicoidal-type structures: competition between nearest and next-nearest neighbor interaction and direct DM interaction, resulting from the loss of a center of symmetry relating magnetic ions. It is easy to show that in none of the magnetic structures described here does the cycloidal modulation lower the symmetric exchange magnetic energy at any order of neighbors, regardless of the sign of the interaction. This suggests that the observed c-axis modulation may be the effect, rather than the cause, of the loss of the center of symmetry relating Mn^{4+} ions.

V. SUMMARY

The magnetic structures in the ferroelectric and/or commensurate magnetic regime of three compounds of the family RMn_2O_5, with $R=$Y, Ho, and Bi, have been determined by single crystal neutron diffraction. For YMn_2O_5 and $HoMn_2O_5$, the main features of the magnetic structures are in agreement with previous models derived from powder neutron diffraction characterized, in particular, by collinear antiferromagnetic zigzag chains in the ab plane. An additional small component of moment parallel to the c axis and modulated in quadrature with the major components has been identified. This component was not detected in earlier experiments. The data also allow a more precise determination of the directions of the Ho magnetic moments. These results indicate the importance of superexchange interactions in the magnetic ordering of Ho. The magnetic structure of $BiMn_2O_5$ is very similar to that of the Y and Ho analogs, but with the magnetic moments more closely confined to the ab plane. It also contains zigzag AFM chains, which is in disagreement with what was previously reported.[22] This comparative study strongly supports symmetric exchange as the principal mechanism leading to ferroelectricity since the small noncollinearity of the magnetic moments within chains along c is observed to a much greater extent for the YMn_2O_5 and $HoMn_2O_5$ compounds. This does not preclude a potential, but much weaker contribution from Dzyaloshinskii-Moriya interactions.

ACKNOWLEDGMENTS

We would like to thank B. Ouladdiaf and G. Mcintyre from the Institut Laue-Langevin (France) for useful discussions and the valuable help during the D10 experiment and the crystal alignment with the OrientExpress instrument. We acknowledge partial support from the European Commission ("Construction of New Infrastructures," ISIS Target Station II, Contract No. 011723). Work at Rutgers was supported by the NSF Grant No. DMR-0520471.

[1] T. Kimura, T. Goto, H. Shintani, K. Ishizaka, T. Arima, and Y. Tokura, Nature (London) **426**, 55 (2003).
[2] N. Hur, S. Park, P. A. Sharma, J. S. Ahn, S. Guha, and S.-W. Cheong, Nature (London) **429**, 392 (2004).
[3] S.-W. Cheong and M. Mostovoy, Nat. Mater. **6**, 13 (2007).
[4] I. Kagomiya, S. Matsumoto, K. Khon, Y. Fukuda, T. Shoubu, H. Kimura, Y. Noda, and N. Ikeda, Ferroelectrics **286**, 889 (2003).
[5] W. Eerenstein, N. D. Mathur, and J. F. Scott, Nature (London) **442**, 759 (2006).
[6] A. F. Garca-Flores, E. Granado, H. Martinho, C. Rettori, E. I. Golovenchits, V. A. Sanina, S. B. Oseroff, S. Park, and S.-W. Cheong, J. Appl. Phys. **101**, 09M106 (2007).
[7] R. Valdés Aguilar, A. B. Sushkov, S. Park, S.-W. Cheong, and H. D. Drew, Phys. Rev. B **74**, 184404 (2006).
[8] Y. Noda *et al.*, Physica B **385**, 119 (2006).
[9] T.-C. Han and J. G. Lin, J. Appl. Phys. **99**, 08J508 (2006).
[10] J. G. Lin, T.-C. Han, and C.-H. Chen, IEEE Trans. Magn. **41**, 3440 (2005).
[11] O. Prokhnenko, R. Feyerherm, E. Dudzik, S. Landsgesell, N. Aliouane, L. C. Chapon, and D. N. Argyriou, Phys. Rev. Lett. **98**, 057206 (2007).
[12] J. Koo *et al.*, Phys. Rev. Lett. **99**, 197601 (2007).
[13] D. I. Khomskii, J. Magn. Magn. Mater. **306**, 1 (2006).
[14] Y. Yamasaki, H. Sagayama, T. Goto, M. Matsuura, K. Hirota, T.

Arima, and Y. Tokura, Phys. Rev. Lett. **98**, 147204 (2007).
[15] G. Lawes *et al.*, Phys. Rev. Lett. **95**, 087205 (2005).
[16] L. C. Chapon, P. G. Radaelli, G. R. Blake, S. Park, and S.-W. Cheong, Phys. Rev. Lett. **96**, 097601 (2006).
[17] I. A. Sergienko, C. Sen, and E. Dagotto, Phys. Rev. Lett. **97**, 227204 (2006).
[18] A. B. Sushkov, R. Valdés Aguilar, S. Park, S-W. Cheong, and H. D. Drew, Phys. Rev. Lett. **98**, 027202 (2007).
[19] C. Wilkinson, F. Sinclair, P. Gardner, J. B. Forsyth, and B. M. R. Wanklyn, J. Phys. C **14**, 1671 (1981).
[20] P. P. Gardner, C. Wilkinson, J. B. Forsyth, and B. M. Wanklyn, J. Phys. C **21**, 5653 (1988).
[21] W. Ratcliff, II, V. Kiryukhin, M. Kenzelmann, S.-H. Lee, R. Erwin, J. Schefer, N. Hur, S. Park, and S-W. Cheong, Phys. Rev. B **72**, 060407 (2005).
[22] A. Muñoz, J. A. Alonso, M. T. Casais, M. J. Martínez-Lope, J. L. Martínez, and M. T. Fernández-Díaz, Phys. Rev. B **65**, 144423 (2002).
[23] H. Kimura, S. Kobayashi, Y. Fukuda, T. Osawa, Y. Kamada, Y. Noda, I. Kagomiya, and K. Kohn, J. Phys. Soc. Jpn. **76**, 074706 (2007).
[24] J. Rodriguez-Carvajal, Physica B **192**, 55 (1993).
[25] G. R. Blake, L. C. Chapon, P. G. Radaelli, S. Park, N. Hur, S-W. Cheong, and J. Rodríguez-Carvajal, Phys. Rev. B **71**, 214402 (2005).
[26] P. G. Radaelli and L. C. Chapon, Phys. Rev. B **76**, 054428 (2007).
[27] J. Pannetier, J. Bassas-Alsina, J. Rodriguez-Carvajal, and V. Caignaert, Nature (London) **346**, 343 (1990).
[28] G. Amoretti, R. Caciuffo, Santini, O. Francescangeli, E. Goremychkin, R. Osborn, G. Calestani, M. Sparpaglione, and L. Bonoldi, Physica C **221**, 227 (1994).
[29] L. C. Chapon, G. R. Blake, M. J. Gutmann, S. Park, N. Hur, P. G. Radaelli, and S-W. Cheong, Phys. Rev. Lett. **93**, 177402 (2004).
[30] C. R. dela Cruz, F. Yen, B. Lorenz, S. Park, S.-W. Cheong, M. M. Gospodinov, W. Ratcliff, J. W. Lynn, and C. W. Chu, J. Appl. Phys. **99**, 08R103 (2006).
[31] H. Katsura, N. Nagaosa, and A. V. Balatsky, Phys. Rev. Lett. **95**, 057205 (2005).
[32] Ionic radius for a valence of 3+ and eight-coordinated configuration.
[33] The $R(F)$ factor is defined as $R(F)=100\{\Sigma_{\mathbf{h}}|F_{obs,\mathbf{h}}-F_{calc,\mathbf{h}}|\}/\{\Sigma_{\mathbf{h}}|F_{obs,\mathbf{h}}|\}$, where F_{obs} and F_{calc} are, respectively, the observed and calculated structure factors for a given reflection **h**.